Full Length Article

Turbulent breakup of non-metallic inclusions and equiaxed crystals during solidification of a hypoeutectic Al-Si alloy

Ewan Lordan [a,*], Kun Dou [a,b], Yijie Zhang [a], Chrysoula Tzileroglou [a], Alain Jacot [a,c], Paul Blake [d], Zhongyun Fan [a]

[a] *Brunel Centre for Advanced Solidification Technology, Brunel University London, Uxbridge, Middlesex, UB83PH, United Kingdom*
[b] *School of Metallurgy and Environment, Central South University, Changsha, Hunan 410083, China*
[c] *Calcom ESI SA, Switzerland*
[d] *Jaguar Land Rover Automotive PLC, Coventry CV3 4LF, United Kingdom*

ARTICLE INFO

ABSTRACT

The breakup of agglomerates and bodies suspended in turbulent flows are important phenomena that influence many aspects of modern solidification processing. It is often assumed that breakup operates in high-pressure die casting, wherein molten metal is transported at high speed through a narrow orifice system. To test this assumption, X-ray tomography and electron backscatter diffraction mapping are used to characterise pores, inclusions, and primary α-Al grains in die-cast samples produced with different flow field intensities. Numerical simulations are performed in ProCAST (ESI Group) to quantify the three-dimensional flow fields and to relate the derived quantities to breakage. Increasing the dissipation rate of turbulent kinetic energy is shown to induce a refinement of both non-metallic inclusions and primary α-Al$_1$ grains nucleated in the shot chamber, a phenomenon which is ascribed to breakage. Several breakup mechanisms are discussed, with emphasis on the role of fluid turbulence.

1. Introduction

The breakup of bodies and aggregates suspended in a turbulent flow are important phenomena that influence many aspects of commercial casting processes. For example, in melt-conditioned direct-chill casting the de-agglomeration of oxide inclusions (e.g. native MgO particles in Mg alloys [1]) creates copious nuclei for heterogeneous nucleation of solidification, which leads to grain refinement [2]. Breakup may also play a prominent role in die-casting processes where defect-forming suspensions, such as gas bubbles [3,4] and oxide films [5], are readily transported by the bulk-liquid flow. Such defects adversely affect the fracture properties of die-cast structures by introducing considerable scatter in the material response [6].

Extrinsic melt treatments are ubiquitously used in foundries to control liquid metal quality prior to solidification processing. These treatments typically utilise an external field to impart a force on the liquid, either directly by agitation [7,8] or indirectly through ultrasonic cavitation [9]. De-agglomeration, in both cases, takes place by a process of erosion, in which particulate matter detaches from the agglomerate surface in response to an external stress [9,10]. Extrinsic melt treatments may not always be appropriate for the solidification process, e.g. in high-pressure die casting (HPDC) the benefits of melt treatment are somewhat

nullified once the liquid is transferred into the shot chamber. Inside the shot chamber, some uncontrolled solidification takes place producing a multi-phase mixture consisting of up to 30 vol.% solid [11]. This multiphase fluid—which carries an array of defect-forming suspensions—is transported at high speeds through a narrow orifice system where it is subject to shear rates in the order of $10^4 \sim 10^5$ s^{-1} [12]. Once the cavity is full, a pressure of $30 \sim 100$ MPa [12] is applied to the solidifying alloy to compress gaseous phases and to assist in the feeding of shrinkage strains. The shear rates during die-filling are of a similar magnitude to those found in melt-conditioning ($10^5 \sim 10^6$ s^{-1} [8]), where breakage has previously been evidenced [3,7,8]. This invites an obvious question: can fluid flow be manipulated in such a way as to promote breakage during the transportation of liquid metals?

Previous studies on breakup in other solid-liquid [13–15] and liquid-liquid [16] systems have revealed how a turbulent field interacts with the disordered structure of an aggregate. An aggregate suspended in a turbulent flow is subject to a hydrodynamic stress that fluctuates intermittently [17]. Viscous forces act on external particles of the aggregate and propagate inwards through a series of inter-particle collisions, causing stress to accumulate in vulnerable branches of the aggregate [18]. When an aggregate is small, with respect to the Kolmogorov length scale, it rotates in the flow like a rigid body and no structural change is observed [13]. Breakup occurs when a turbulent oscillation is

---

violent enough to generate an internal stress that exceeds the cohesive strength of the inter-particle bonds, releasing a small fragment of the aggregate into the liquid [14,15,17–20]. Several researchers posit that the shear rates during die filling are large enough to incite aggregate breakage [21], dendrite fragmentation [22] and bubble disintegration [4,21]; however, many of the ideas in these papers appear to be incomplete. In light of such claims, it would be interesting to investigate the effect of fluid turbulence on the size, shape, and spatial distribution of defects in die-cast materials.

An *in-situ* study of turbulent breakup in metallic alloy systems is presently unfeasible. Liquid metals are opaque, preventing the use of optical techniques such as particle tracking velocimetry; synchrotron X-ray imaging does not possess the spatial or temporal requirements for a study of turbulence. One must, therefore, infer the existence of breakage from observation of the as-cast microstructure. In this work, X-ray tomography, unsupervised machine learning, and electron backscatter diffraction (EBSD) mapping are used to characterise pores, inclusions, and equiaxed grains in die-cast samples produced with different flow field intensities. Numerical simulations are performed in ProCAST (ESI Group) to quantify the three-dimensional flow fields and to relate the derived quantities to breakage. We demonstrate that higher flow field intensities promote breakage, enhancing the tensile properties of the casting. These findings present unique opportunities for both scientific and technological development, particularly in the sphere of die design.

2. Experimental

2.1. Specimen preparation

LM24 alloy (8.09 wt.% Si, 3.11 wt.% Cu, 1.78 wt.% Zn, 0.86 wt.% Fe, 0.22 wt.% Mn, 0.16 wt.% Mg and 0.04 wt.% Ti) supplied by Norton UK was used as a base material. The melt was degassed using a commercial rotary degassing unit and then manually poured into the shot chamber of a Frech 4500 kN locking force cold chamber HPDC machine. The pouring temperature, die temperature and shot chamber temperature were maintained at 680 °C, 200 °C and 180 °C, respectively. Fig. 1 presents the two dies used to produce ASTM standard E8/E8M tensile specimens [23]. The two dies differ in their choice of runner system: one adopts a traditional runner system (TRS), the other employs a lean runner system (LRS) that accelerates the liquid through a contractile flow. The plunger kinematics were fixed during the experiments, with notable speeds of 0.3 ms^{-1} and 3.6 ms^{-1} for the slow-shot and die-filling stages, respectively.

2.2. Tensile testing and SEM fractography

Tensile tests were performed at ambient temperature using an Instron 5500 universal electromechanical testing system, in accordance with ASTM standard E8/E8M [23]. The gauge length and gauge diameter of the tensile specimens are 55 mm and 6.35 mm, respectively. Tensile data was recorded using a 50 mm extensometer with a ramp rate of 1 mm/min. Fractographic examinations were carried out using a LEO 1455VP (Carl Zeiss AG) scanning electron microscope (SEM) equipped with energy-dispersive X-ray spectroscopy (EDX).

2.3. X-ray tomography

X-ray tomography was performed using a Xradia 410 Versa (Carl Zeiss AG) computed tomography system operated at 80 kV and 10 W; an isotropic voxel was defined with an approximate length scale of 3.5 μm. The VGSTUDIO MAX software suite (Volume Graphics GmbH) was used to visualise and analyse the three-dimensional volumes. An iterative surface determination was performed to isolate the material volume while compensating for local fluctuations in grey value. Quantitative measures of defect size and morphology were obtained using the VGDEFX Void and Inclusion Analysis module in VGSTUDIO MAX. A minimum volume
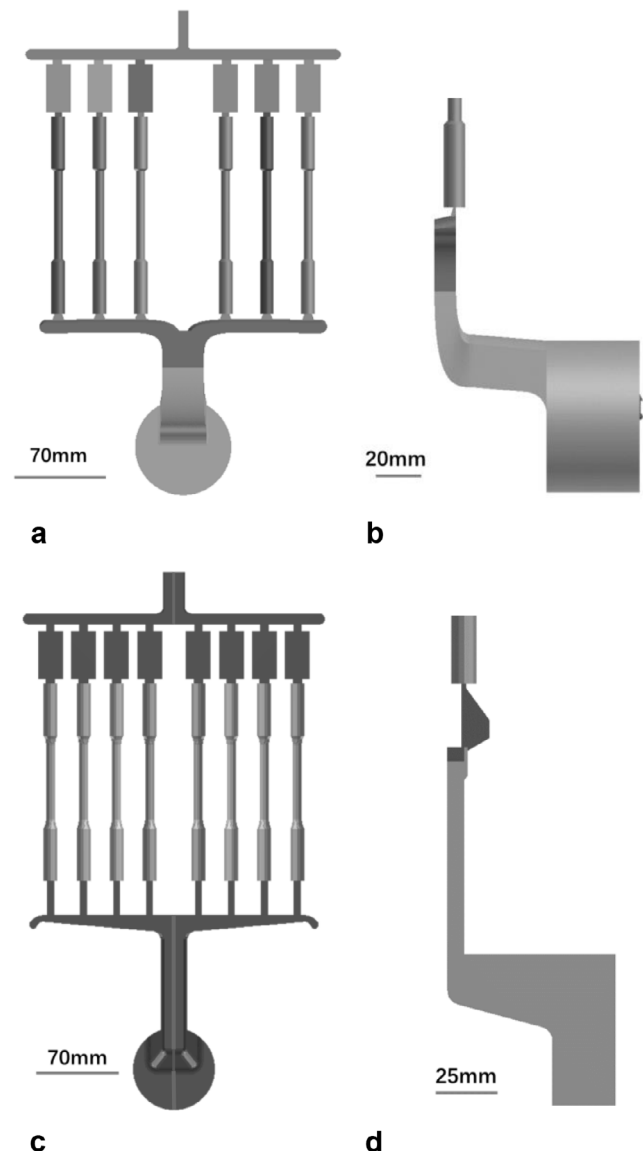

Fig. 1. Dies used to produce ASTM standard E8/E8M [23] tensile specimens: (a,b) the TRS die, which employs a conventional runner system; (c,d) the LRS die, which accelerates the liquid through a contractile flow. Shown in (b) and (d) are side views of the TRS and LRS, respectively.

of 8 voxels was defined as a threshold for the analysis. Defects in this work are on average ~100 μm in diameter. The voxel size of 3.5 μm is thus assumed to have a marginal effect on the characterisation of pores and inclusions in this work.

2.4. EBSD mapping

Samples for EBSD were sectioned from the centre of the gauge length, transverse to the bulk flow direction. Samples were prepared to a 0.04 μm finish using standard metallographic techniques, and then subject to vibratory polishing for 40 min with a frequency of 90 Hz. EBSD was carried out on a Crossbeam 350 FIB-SEM (Carl Zeiss AG) equipped with an EDAX EBSD analyser (EDAX Inc.). EBSD data was acquired at 20 kV with a sample tilt of 70 °. Mapping was performed using the TEAM Software package (EDAX Inc.), for which a 152×120 μm region was analysed with a step size of 0.4 μm; this step size ensures a minimum of 6 pixels per grain width, in accordance with previous studies [24]. After mapping, EBSD data was analysed in the OIM Analysis software (EDAX Inc.).
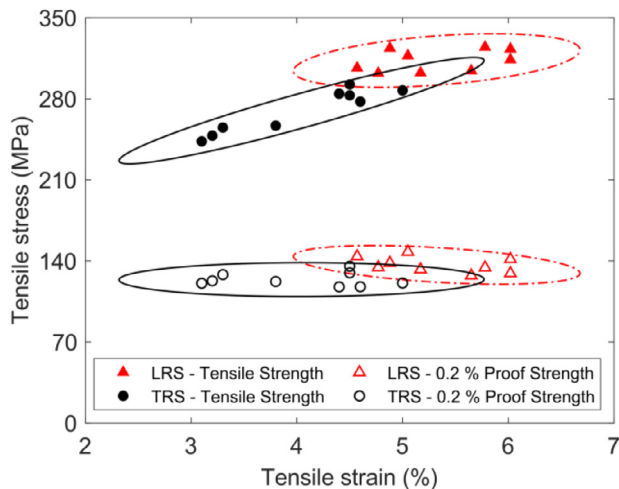
Fig. 2. Tensile properties and associated 95% confidence ellipses for two-dimensional normally distributed data.

2.5. Numerical modelling

The HPDC process was simulated using a finite element model developed under the ProCAST (ESI Group) software platform. Details of the modelling procedure are outlined in our previous paper [25]. In short, governing equations for mass, momentum, and heat (based on the enthalpy method) are solved in ProCAST [25]. The volume of fluid (VOF) method is used to monitor the evolution of the melt free surface [25]. Fluid turbulence is described using a standard k-ε turbulence model described in references [26–28]. Simulations were performed on finite element meshes generated for the TRS and LRS dies using geometrical models produced in AutoCAD (Autodesk Inc.).

3. Results

3.1. Tensile properties

Fig. 2 presents the tensile properties of specimens produced with the TRS and LRS dies; 95% confidence ellipses are shown for two-dimensional normally distributed data. The tensile properties of LRS specimens are on average higher than those of TRS specimens. For example, average values of $4.0 \pm 0.7\%$ and $6.7 \pm 0.6\%$ are obtained for the tensile ductility of TRS and LRS specimens, respectively. The increase in tensile strength and 0.2% proof strength is more modest in comparison, with average values of 270 ± 19 MPa and 313 ± 9 MPa, and 124 ± 6 MPa and 137 ± 7 MPa obtained for the TRS and LRS specimens, respectively. Similar trends have previously been reported by Gunasegaram et al. [21] for a wider range of flow field intensities.

3.2. X-ray tomography

3.2.1. Inclusions

Fig. 3 shows a visualisation of inclusions in the TRS and LRS samples, produced via X-ray tomography. Inclusion size was determined using the maximum Feret diameter method (the distance between two parallel tangential planes enclosing the largest dimension of the particle or void). Future reference to particle size will also imply use of the maximum Feret diameter method, with the diameter denoted by D. Inclusions in the LRS sample are on average smaller than those in the TRS sample, with average diameters of 0.09 ± 0.03 mm (max. 0.37 mm) and 0.15 ± 0.08 mm (max. 0.73 mm), respectively. However, the difference between the means is modest compared to that of the maximum values. Fig. 3(c) presents the probability distributions of inclusion size for the two materials. Although the modal values are relatively similar, there

is a marked difference in the tails of the two distributions. Inclusions in the LRS sample also possess a more compact morphology than those in the TRS sample, with average compactness values of 0.28 ± 0.12 and 0.20 ± 0.11 obtained for each material, respectively. Here, compactness refers to the ratio V_i/V_s, where V_i is the volume of the inclusion and V_s the volume of its enclosing sphere. Values of compactness lie between zero and unity, with low values indicative of irregular morphology. Regarding their spatial distribution, inclusions are more uniformly distributed in the LRS sample compared to the TRS sample.

3.2.2. Porosity

Fig. 4(a,b) shows a visualisation of pores in the TRS and LRS samples, produced via X-ray tomography; corresponding size distributions are shown in Fig. 4(c). The average pore sizes are relatively similar, with values of 0.08 ± 0.02 mm (max. 0.28 mm) and 0.07 ± 0.04 mm (max. 0.40 mm) reported for the TRS and LRS samples, respectively. Pores in both samples are highly spherical, with average sphericities of 0.61 ± 0.05 and 0.61 ± 0.07 reported for the TRS and LRS samples, respectively. The spherical nature of these pores suggest that they originate from gaseous sources as opposed to solidification shrinkage [6]. Micropores in both samples are located towards the centreline flow, mimicking the shape of a conical screw. In contrast, large pores (0.2~0.4 mm) are randomly distributed in space, again implying gaseous origins: one would expect shrinkage pores to congregate in the central core [6].

3.3. Grain size

Fig. 5(a,b) shows inverse pole figure (IPF) maps for the TRS and LRS samples, produced via EBSD mapping. The grain structure appears to comprise a mixture of large dendritic primary α-Al$_1$ grains (30~150 μm) nucleated in the shot chamber, and smaller globular rosette primary α-Al$_2$ grains (3~10 μm) nucleated in the die cavity. Such differences in size and morphology may be ascribed to the low cooling rates in the shot chamber ($\sim$10 Ks^{-1} [29]) compared to those in the die cavity (500~1000 Ks^{-1} [29]). Fig. 5(c,d) shows grain size distributions corresponding to the IPF maps in Fig. 5(a,b). Grain size distributions are often observed to approximate a lognormal shape, a phenomenon that has previously been ascribed to the time-dependant kinetics of crystal growth processes [30]. Accordingly, we present grain size in terms of its natural logarithm (i.e. $\ln D$). Both distributions are multimodal, an observation that is more pronounced in the TRS distribution than in the LRS distribution. Further discussion regarding grain size is deferred to Section 4.3.

3.4. Numerical modelling

Numerical simulations were performed in ProCAST to quantify the three-dimensional flow fields and to relate the derived quantities to breakage. Fig. 6 compares the dissipation rate of turbulent kinetic energy (ε) along the flow path of the two dies. Higher levels of ε are observed in the LRS than in the TRS. Moreover, the melt is exposed to this high energy flow for a prolonged period in the LRS due to its increased pipe length. In both dies, the melt experiences high ε just upstream of the orifice system, the intensity of which varies with position: the initial jets quickly traverse the length of the die, reaching the far wall before filling back towards the orifice system, impeding the flow of newly arriving fluid [31]. In the TRS die, high levels of ε are observed downstream of certain orifices, a phenomenon that is not observed in the LRS die. This is likely due to the abrupt orifice design in the TRS die (Fig. 1(b)). In contrast the LRS die employs a flow buffer (Fig. 1(d)) that dampens turbulence prior to die-filling.

Fig. 7 compares the melt temperature in the two castings at the end of die-filling. The average melt temperature in the LRS casting is below the liquidus temperature of the alloy (614 ^{0}C, calculated using a database supported by the ESI Group [28]); the lean geometry of the
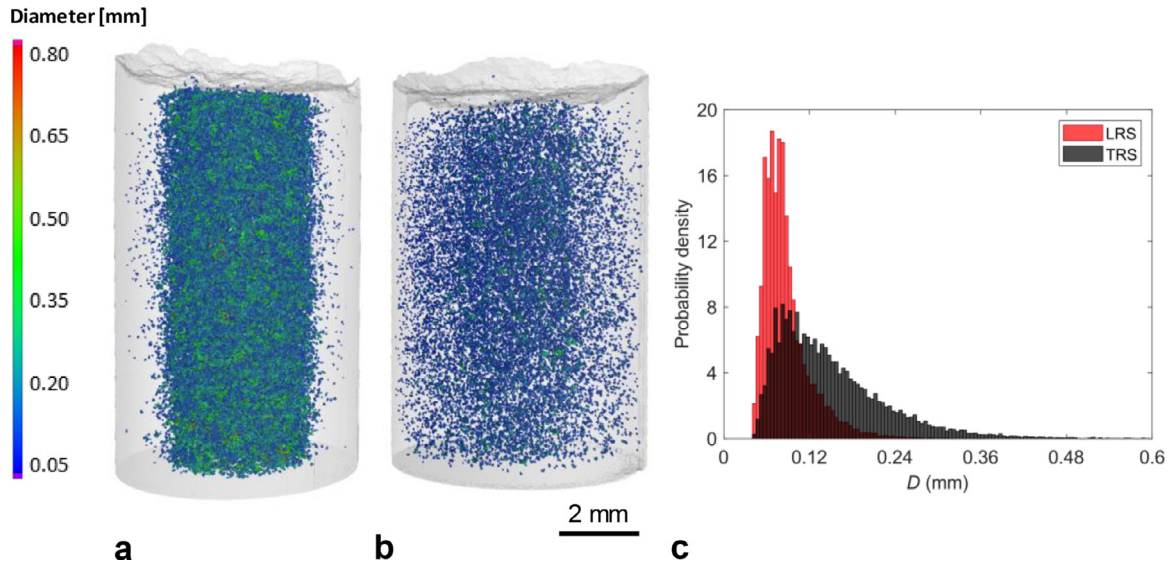
Fig. 3. Three-dimensional visualisation of inclusions within each sample, produced via X-ray tomography: (a) TRS sample, (b) LRS sample, and (c) corresponding size distributions.
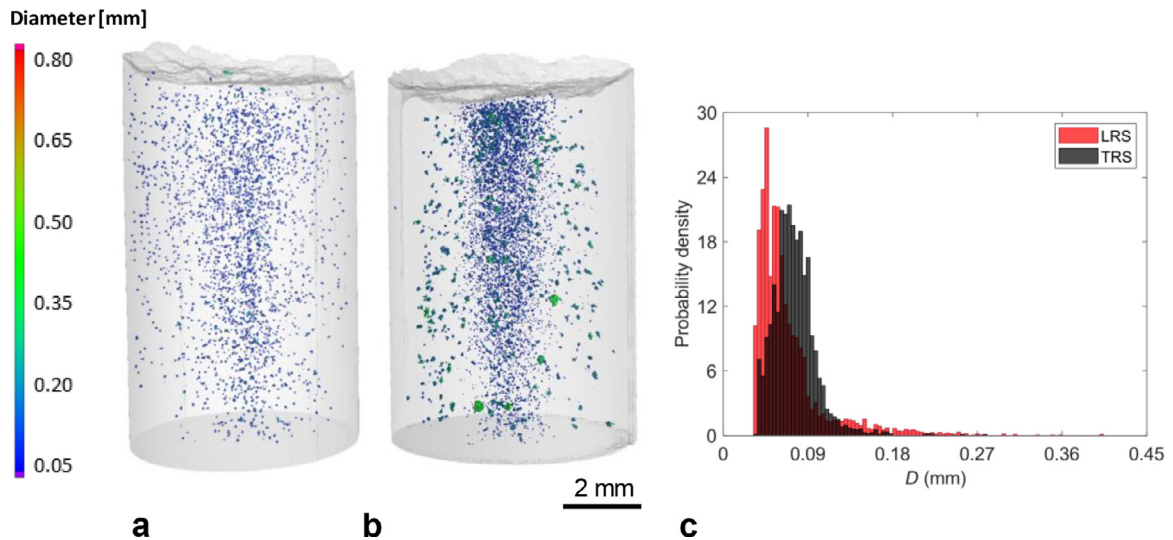

Fig. 4. Three-dimensional visualisation of pores within each sample, produced via Xray tomography: (a) TRS sample, (b) LRS sample, and (c) corresponding size distributions.

LRS is shown to promote heat extraction, leading to higher cooling rates during solidification.

4. Discussion

4.1. Statistical modelling of extreme values

4.1.1. The generalized pareto distribution

Although the average inclusion/pore sizes presented in Section 3.2 are relatively similar, there is a marked difference in the tails of the distributions. Accordingly, a peaks-over threshold approach was used to model tail data. We regard as extreme events those observations $x_1, \ldots, x_n$ that exceed some threshold u. Thus, for sufficiently large u, the distribution of threshold exceedances $y_i = x_i - u$ is approximately

$$H(y) = 1 - \left(1 + \frac{\xi y}{\tilde{\sigma}}\right)^{-1/\xi} \tag{1}$$

for $y > 0$ and $(1 + \xi y/\tilde{\sigma}) > 0$ [32]. The family of continuous distributions defined by Eq. (1) are collectively known as the generalized Pareto (GP) distribution. The GP distribution is parameterized by a scale parameter $\tilde{\sigma}$ and a shape parameter ξ. The shape parameter ξ controls the tail behaviour of the distribution: $\xi < 0$ implies an underlying distribution with a finite upper bound $(u - \tilde{\sigma}/\xi)$; $\xi > 0$ gives a boundless distribution with a polynomially decreasing tail; $\xi \to 0$ is equivalent to an exponential distribution with rate $1/\tilde{\sigma}$. A suitable threshold u was determined for each data set using the threshold stability property of the GP distribution. Parameter estimates were obtained by maximum likelihood estimation using the Statistics and Machine Learning Toolbox™ in MATLAB (Mathworks). The mth-observation return level X_m was then obtained by inverting Eq. (1) for $\Pr(X_m > x | X_m > u) = 1/m$.

4.1.2. Inclusions

The GP function was used to model the upper tail of the inclusion size distributions shown in Fig. 3(c). Diagnostic plots are provided in the supplementary material (Figs. S1 and S2); parameter estimates for the fitted distributions are shown in Table 1. The threshold u of the
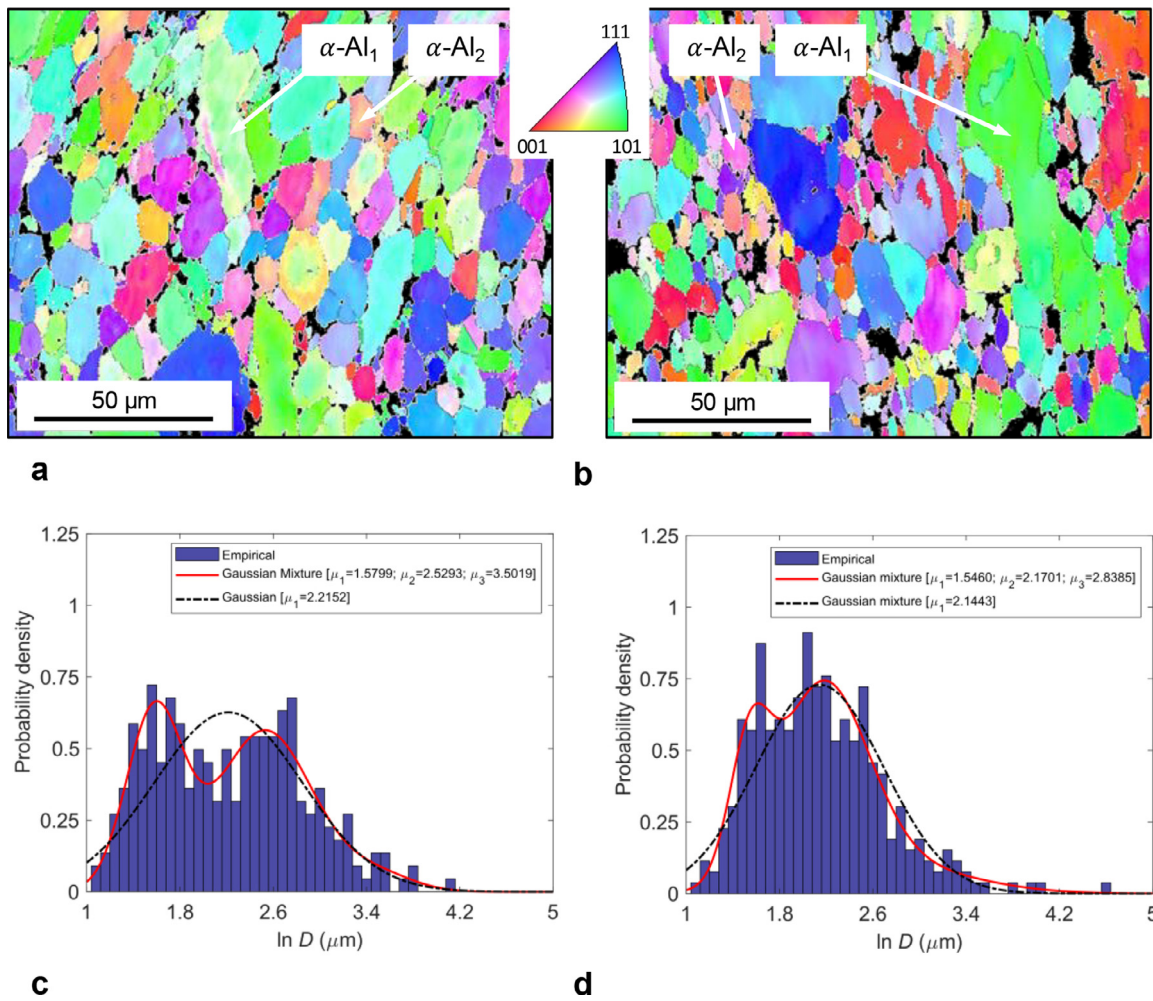
Fig. 5. EBSD mapping of primary α-Al grains in the (a,c) TRS, and (b,d) LRS samples. Shown are IPF maps (a,b), and corresponding size distributions (c,d). Gaussian functions and Gaussian mixture models are shown as dashpot lines and solid lines in (c,d), respectively. Mapping was performed in the [001] reference direction.
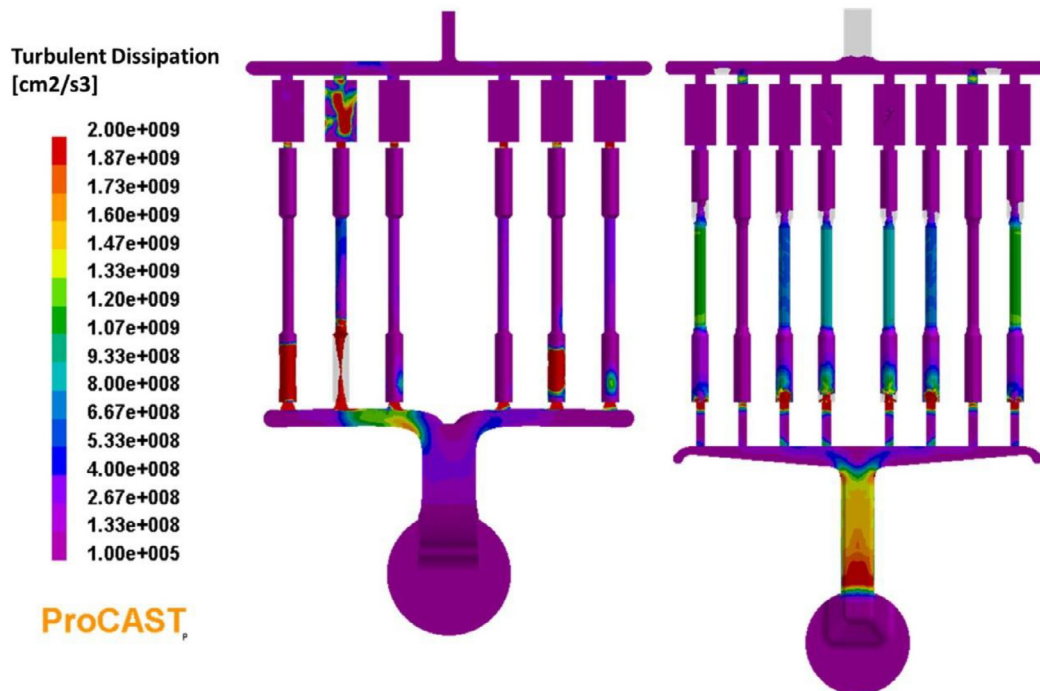

Fig. 6. Turbulent energy dissipation rate along the flow path of the TRS (left) and LRS (right) dies; numerical simulations were performed using ProCAST code.
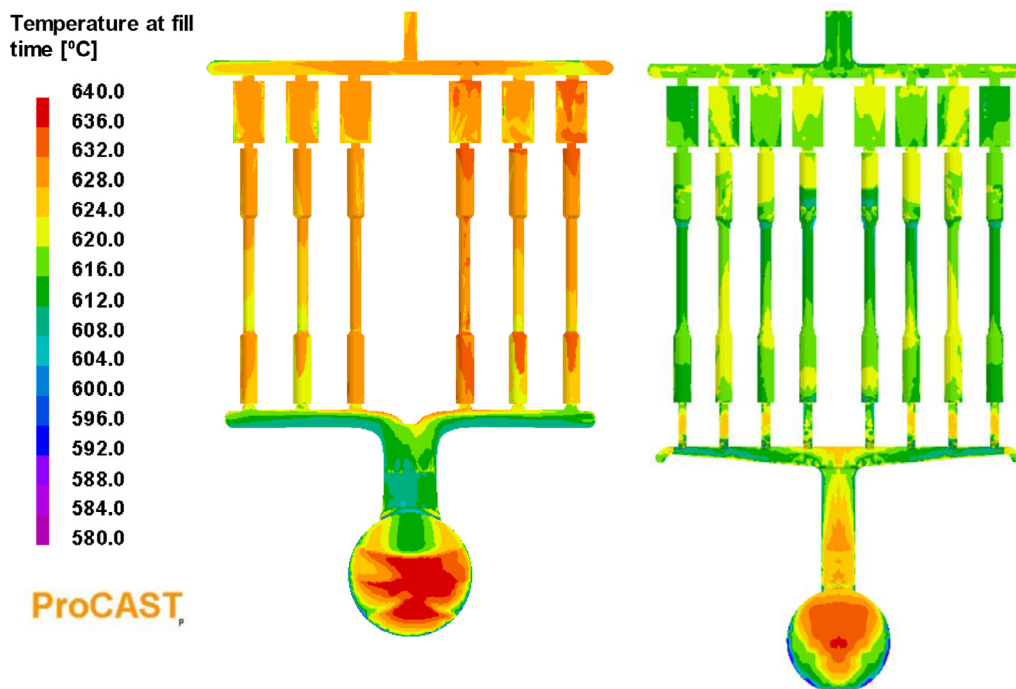
Fig. 7. ProCAST simulations depicting melt temperature at the end of die filling, for the TRS (left) and LRS (right) castings.
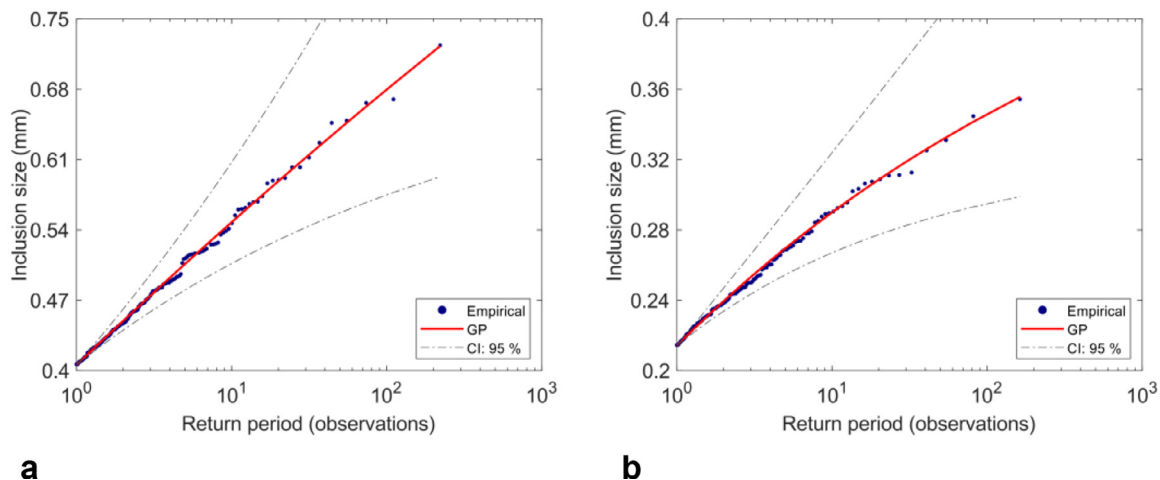

Fig. 8. Predicted (GP) values of inclusion size for the (a) TRS, and (b) LRS samples. The GP curve was calculated by inverting Eq. (1) for Pr $(X_m > x \,|X_m > u) = 1/m$. It thus represents a lower bound to the maximum inclusion size expected in a group of m observations. For comparison, experimental values of inclusion size are plotted in ascending order (Empirical). The dashpot lines represent 95% confidence intervals (CI: 95%) calculated using values from Table 1. Note that the scale of the ordinate differs in (a) and (b).

Table 1
GP parameters used to model the upper tails of the inclusion size distributions shown in Fig. 3(c).

	ξ− Mean	ξ− 95% Confidence Intervals	$\tilde{\sigma}$	u	X_{10} (mm)
TRS	−0.032	[−0.169; 0.106]	0.064	0.406	0.548
LRS	−0.132	[−0.276; 0.012]	0.031	0.214	0.290

TRS distribution is significantly larger than that of the LRS distribution. There is also a notable difference in the tail behaviour of the two distributions. For example, the negative shape parameter ξ = - 0.132 implies that the LRS distribution possesses a finite upper bound of ∼0.49 mm. In contrast, $\xi \rightarrow 0$ implies that the TRS distribution is boundless. The return level plots in Fig. 8 exemplify this disparity. Moreover, the 10th-observation return level X_{10} for the TRS distribution exceeds the upper bound of the LRS distribution. In fact, ∼22% of inclusions in the TRS material are larger than the largest inclusion in the LRS material (the return period m associated with $X_m = 0.49$ mm is ∼4.5 for the TRS distribution).

4.1.3. Porosity

GP distributions were fitted to the pore size distributions shown in Fig. 4(c). Diagnostic plots are provided in the supplementary material (Figs. S3 and S4). Estimates of the GP parameters are shown in Table 2. Return level plots for the fitted distributions are shown in Fig. 9. Although the thresholds u are relatively similar, differences between the two distributions become more apparent as m increases (illustrated by the values of X_{10}). Suppose these pores originate from gaseous sources, as per Section 3.2.2. It follows that the flow constriction in the LRS
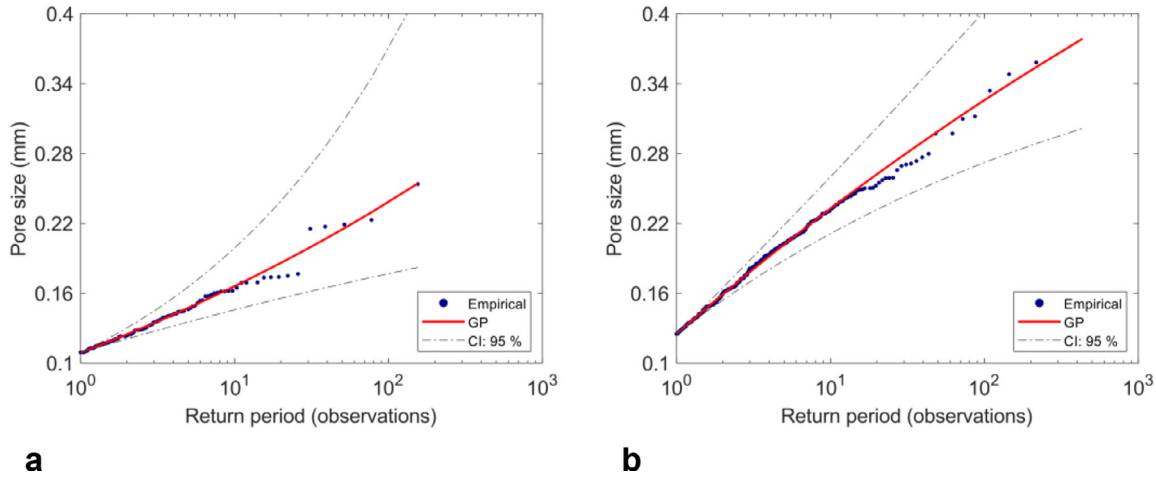
Fig. 9. Predicted (GP) values of pore size for the (a) TRS, and (b) LRS samples. The GP curve was calculated by inverting Eq. (1) for $\Pr\left(X_m > x\mid X_m > u\right) = 1/m$. It thus represents a lower bound to the maximum pore size expected in a group of m observations. For comparison, experimental values of pore size are plotted in ascending order (Empirical). The dashpot lines represent 95% confidence intervals (CI: 95%) calculated using values from Table 2.

Table 2
GP parameters used to model the upper tails of the pore size distributions in Fig. 4(c).

	$\xi-$ Mean	$\xi-$ 95% Confidence Intervals	$\tilde{\sigma}$	u	X_{10} (mm)
TRS	0.103	[−0.074; 0.279]	0.017	0.109	0.166
LRS	−0.063	[−0.149; 0.024]	0.050	0.125	0.233

leads to an increase in pore size. Several researchers [4,21] assert the contrary, i.e. higher melt speeds result in a smaller pore size due to the dispersion of gas bubbles. However, these assertions assume that most of the gas bubbles are introduced prior to die-filling. When a bubble is placed in a turbulent field, it oscillates and deforms due to fluctuations of the local pressure gradient. Breakup occurs when the kinetic energy transmitted by a turbulent event is greater than the surface energy of the bubble [33]. Although the flow buffer in the LRS die (Fig. 1(d)) reduces turbulence downstream of the orifice, an appreciable increase in ε is observed in the gauge length of the tensile specimens (Fig. 6). It is possible that either this ε is less than the critical value ε_{crit} required for breakage, or that the filling times involved in HPDC (10~100 ms [34]) are too small to facilitate breakage inside the cavity. When $\varepsilon < \varepsilon_{crit}$, or when the particle residence time is too short, turbulence may promote air entrapment and bubble coalescence, driving an increase in pore size.

4.1.4. Improvement in mechanical properties

Significant improvements in tensile ductility were obtained by promoting turbulence in the runner system (Fig. 2)—but what causes this improvement? Few oxides were observed on the fracture surface of the tensile specimens, and when they were observed they were negligible in size (~50 μm); no other abnormalities were observed on the fracture surfaces of the tensile specimens. This indicates that oxides are not responsible for the low ductility of the TRS specimens. Comparing the return levels X_{10} obtained from the extreme value analysis (Tables 1 and 2), an increase in ε is accompanied by a significant decrease in inclusion size and a moderate increase in pore size. Additionally, in both materials the value of X_{10} obtained for the inclusion size distribution exceeds that of the pore size distribution. This suggests that the observed improvement in tensile properties is due to a refinement of large inclusions in the LRS. Strain localises at these defects, causing failure to occur at stresses below the theoretical strength of the material. Thus, the joint increase in tensile strength and tensile ductility (Fig. 2) does not contradict strengthening theory: the theoretical strength of the material is constant. On a separate note, tensile ductility deteriorates more rapidly

in the presence of a defect than tensile strength [6]. This explains why the increase in tensile strength (mean: +16%) is less than that for tensile ductility (mean: +68%). It also accounts for the relatively high strength of the alloys, despite the presence of inclusions and gas pores.

4.2. Breakup of non-metallic inclusions

4.2.1. Gaussian mixture models

Next, we discuss the mechanism by which inclusions are refined in the LRS. We begin by deducing the species of inclusions contained in the X-ray tomography data sets. The size and morphology of an inclusion will vary depending on the local thermal and hydrodynamic conditions. In an unstirred melt, these features will fluctuate about some mean value unique to that species of inclusion. As ε increases, we suspect that breakage will induce both refinement and morphological change, i.e. inclusions will become smaller in size and more compact in morphology. Clustering is a canonical problem in unsupervised machine learning, in which query data is partitioned into groups, or clusters, based on similitude. In a Gaussian mixture model (GMM), clusters are modelled as a mixture of normal density components. The mixture density function is given by a weighted linear combination of the k - component densities [35]:

$$F(x) = \sum_{i=1}^{k} \alpha_i f\left(x \mid \boldsymbol{\mu}_i,\ \boldsymbol{\Sigma}_i\right),$$
$$f\left(x \mid \boldsymbol{\mu}_i,\ \boldsymbol{\Sigma}_i\right) = \frac{1}{\sqrt{(2\pi)^n |\boldsymbol{\Sigma}_i|}} \exp\left(-\frac{1}{2}\left(x - \boldsymbol{\mu}_i\right)^T \boldsymbol{\Sigma}_i^{-1}\left(x - \boldsymbol{\mu}_i\right)\right) \tag{2}$$
$$\sum_{i=1}^{k} \alpha_i = 1$$

where x is our n-dimensional feature vector and $\{\alpha_i, \boldsymbol{\mu}_i,\ \boldsymbol{\Sigma}_i\}$ denote the mixture weight, mean vector and covariance matrix associated with each component density $f(x \mid \boldsymbol{\mu}_i,\ \boldsymbol{\Sigma}_i)$, respectively.

Multivariate GMMs were fitted to the inclusion populations shown in Fig. 3. An n-dimensional feature vector x was defined, with each row containing values for the diameter (D), compactness and mean grey value of a given inclusion. The mean grey value represents the attenuation of the X-ray beam averaged over all pixels of the inclusion. Parameter estimates for the GMM were obtained by expectation-maximization using the Statistics and Machine Learning Toolbox™ in MATLAB. Values of k were determined empirically using the Akaike information criterion (AIC) and the Bayesian information criterion (BIC). Estimated AIC and BIC for the two inclusion populations are shown in the supplementary material (Fig. S5) and support the case of $k = 3$. Each mixture component is equivalent to a three-dimensional normal distribution with mean vector $\boldsymbol{\mu}_i$ and covariance matrix $\boldsymbol{\Sigma}_i$, which may be visualised as
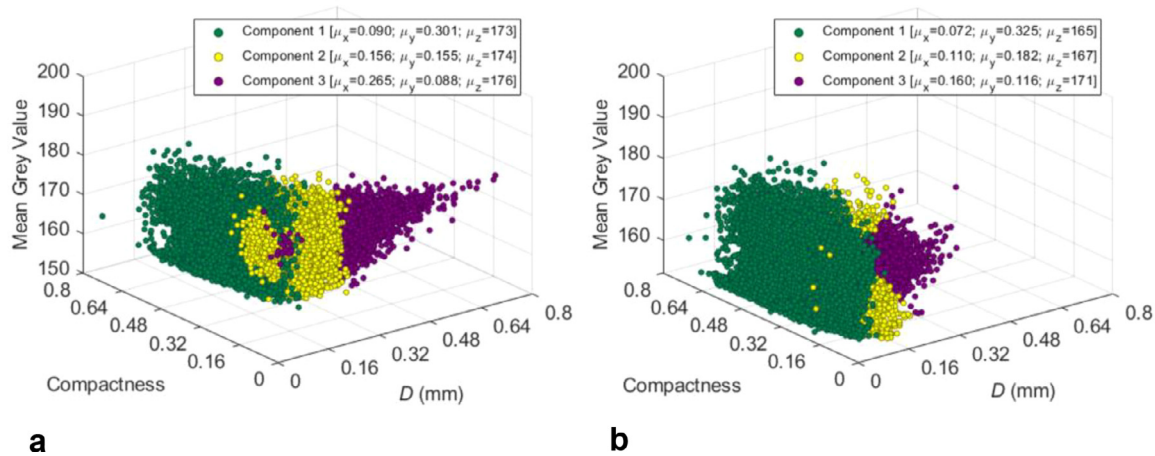
Fig. 10. Multivariate GMMs ($k = 3$) fitted to X-ray tomography data obtained for (a) the TRS sample, and (b) the LRS sample. The x, y, and z axes denote the diameter (D), compactness, and mean grey value of each inclusion identified by the VGDEFX algorithm, respectively.

an ellipsoid. In Fig. 10 each inclusion is assigned to one of three clusters according to its posterior probabilities, i.e. the probability that the data point belongs to a given cluster.

4.2.2. Species of inclusions

So far, we have partitioned inclusions into three clusters based on their size, shape and attenuating behaviour. The question we wish to address is: what species of inclusions do these clusters represent? Consider the mean vector of each component in the TRS mixture model: $\boldsymbol{\mu}_1 = \langle 0.090, 0.301, 173 \rangle$, $\boldsymbol{\mu}_2 = \langle 0.156, 0.155, 174 \rangle$, $\boldsymbol{\mu}_3 = \langle 0.265, 0.088, 176 \rangle$. Candidate inclusions must be of a comparable size to the mean diameter μ_x of the cluster; the morphology of these inclusions must also relate to the mean compactness μ_y of the cluster. Additionally, there must be enough atomic contrast between the inclusion and Al-matrix to produce a detectable increase in X-ray attenuation. The phase diagram (see Fig. S6 in the supplementary material) presents two intermetallic phases as candidates: α-Al$_{15}$(FeMn)$_3$Si$_2$ and β-AlFeSi. In HPDC, two-types of α-Al$_{15}$(FeMn)$_3$Si$_2$ phase precipitate during solidification: primary α-Al$_{15}$(FeMn)$_3$Si$_2$ phase forms in the shot chamber, exhibiting a polyhedral/Chinese script morphology (20~100 μm [36]); proeutectic α-Al$_{15}$(FeMn)$_3$Si$_2$ phase forms in the die cavity, exhibiting a compact polyhedral morphology (3~20 μm [36]). The appreciable difference in size is due to the high cooling rates in the die cavity ($\sim$1000 Ks^{-1} [29]) compared to that in the shot chamber ($\sim$10 Ks^{-1} [29]). Clearly, the proeutectic α-Al$_{15}$(FeMn)$_3$Si$_2$ phase is outside the spatial resolution of the X-ray tomography scan. Furthermore, β-AlFeSi phases are rarely observed in the two materials (see Fig. S7 in the supplementary material): this is attributed to the addition of Mn which acts to suppress the formation of β-AlFeSi [37].

Large non-metallic inclusions are also present in both materials; representative micrographs of these inclusions are shown in Fig. 11. EDX analysis revealed that these inclusions typically contain C, Na, S, Cl, K, and Ca—the latter two elements are of interest, as they fulfil the atomic contrast requirement for X-ray tomography. The fact that these inclusions contain K and Ca does not necessarily mean that they will be more attenuating than the aforementioned Fe-rich phases, particularly if these elements are distributed in a diffuse manner or if the inclusions possess a film-like morphology. Comparing the mean grey values μ_z of each cluster in the TRS mixture model (Fig. 10), inclusions in Component-2 (174) and Component-3 (176) are, on average, more attenuating than those in Component-1 (173). However, a more notable difference lies in the spread of the mean grey values within each cluster. For example, Component-1 and Component-2 both exhibit a wide range of mean grey values (150~180) within a relatively small size interval (100~300 μm). Conversely, inclusions in Component-3 appear to attenuate in a more

consistent manner, with the mean grey value observed to increase with an increase in inclusion size. This suggests that Component-3 represents a single species of inclusion, while Component-1 and Component-2 comprise a mixture of non-metallic inclusions and intermetallic phases.

Oil-based lubricants are often applied to the plunger tip to prevent wear and seizure. Petrochemical or synthetic based additives are often added to base stocks to impart additional properties to the lubricant. Extreme pressure additives enhance lubricity in high-pressure environments, and often contain compounds of S or Cl [38]. Other additives, such as surfactants and thickeners, are also used in commercial lubricants, and often contain compounds of Na, K and Ca [39]. These elements are consistent with those in the EDX spectrum in Fig. 11. When molten metal is poured into the shot chamber, it reacts with organic compounds contained in the plunger lubricant to produce gaseous phases and a carbonaceous residue—this pyrolysis presents itself as a flame emerging from the pouring hole. It is possible that this residue is entrained into the liquid during die-filling, materialising as non-metallic inclusions in the residual microstructure; however, further work is required to test this hypothesis.

4.2.3. Influence of ε on breakage

Previously, we narrowed our candidate inclusions down to primary α-Al$_{15}$(FeMn)$_3$Si$_2$ phase, β-AlFeSi phase, and non-metallic inclusions. Fig. 11 shows that these non-metallic inclusions vary significantly in both size (100~800 μm) and morphology (compact to highly irregular). Since high levels of ε are attained in both dies (Fig. 6), breakage should be evidenced in both materials. From Section 4.2.2, we infer that Component-3 is composed entirely of large non-metallic inclusions. Additionally, we infer that Component-1 consists of primary α-Al$_{15}$(FeMn)$_3$Si$_2$ phase solidified in the shot chamber and fine non-metallic inclusions. Component-2 is expected to comprise a mixture of fine non-metallic inclusions and β-AlFeSi phases. Comparing the mean vectors of the two mixture models, an increase in ε is accompanied by a decrease in the mean diameter μ_x and an increase in the mean compactness μ_y of all three clusters—an effect which is most notable in Component-3. Additionally, the probability density contours in Fig. 12 shows that the peaks of the LRS mixture model also move towards a region of higher compactness and lower diameter compared to the TRS model. In fact, the number fraction of inclusions in Component-1 of the LRS mixture model (0.65) is approximately double that of the TRS mixture model (0.32). Thus, increasing ε and/or the particle residence time leads to a refinement of large non-metallic inclusions and the production of small, compact particles. Since solidification conditions in the shot chamber were closely monitored, it is proposed that the production of fines is attributed to the breakup of non-metallic inclusions. This sup-
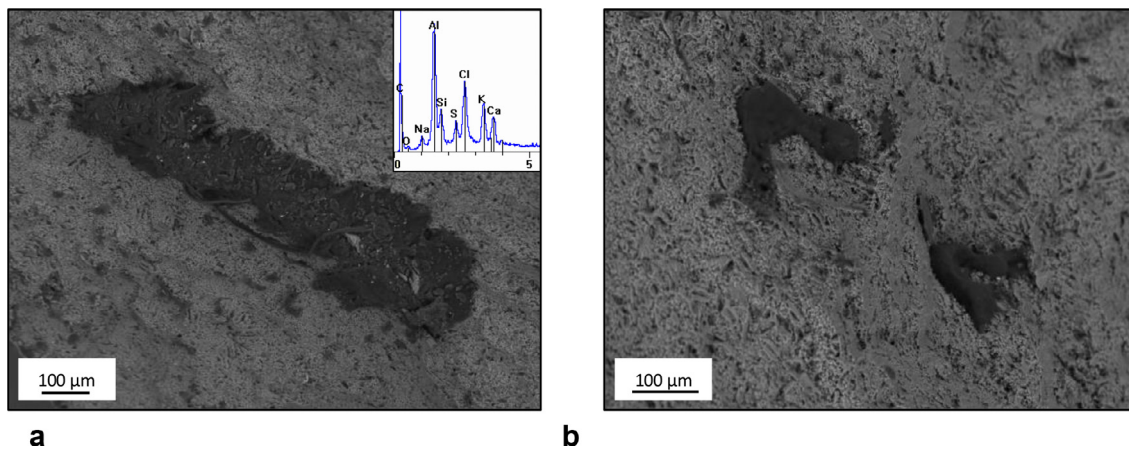
Fig. 11. SEM micrographs of non-metallic inclusions observed on the fracture surface of tensile specimens. (a) large inclusion with an irregular morphology; (b) fine, compact inclusions. The inset in (a) shows a representative EDX spectrum for these non-metallic inclusions. Both images were acquired by detecting backscattered electrons in the SEM.
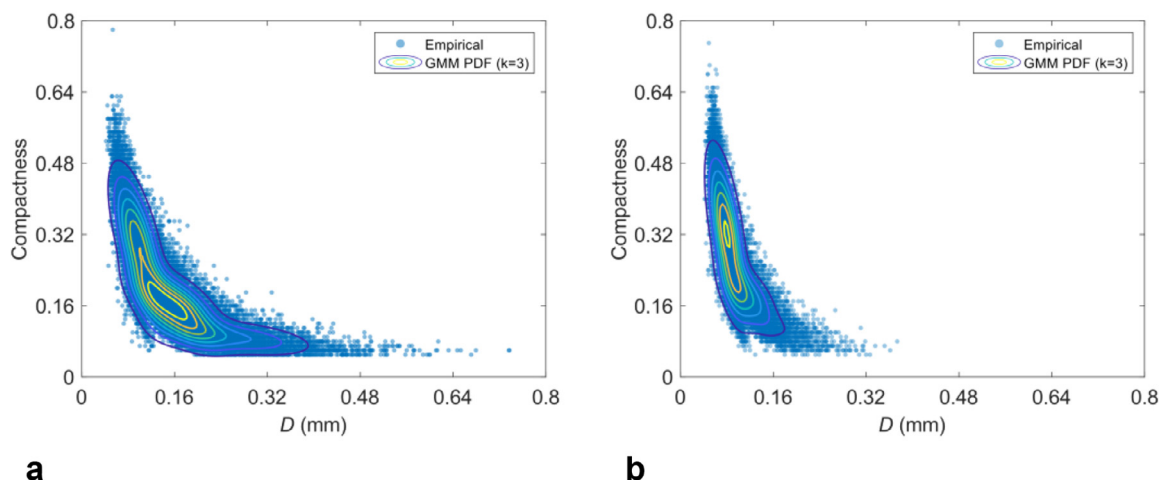
Fig. 12. Multivariate GMMs ($k = 3$) fitted to X-ray tomography data obtained for the (a) TRS, and (b) LRS samples. Shown are probability density contours for a projection of the three-dimensional model in Fig. 10.

position is supported by the mean grey values observed in Component-1 (Fig. 10): although the number of inclusions with mean grey values in the range 150~160 remains relatively constant, an increase in ε is accompanied by a significant increase in the number of inclusions with mean grey values of 160~180. It is proposed that these non-metallic inclusions break apart in a manner analogous to the fragmentation of solid aggregates [13,14] and highly viscous droplets [16] suspended in a turbulent flow.

4.3. Crystal fragmentation

There is a growing consensus that grain size distributions in HPDC microstructures are bimodal, i.e. they comprise a mixture of large dendritic α-Al$_1$ grains (30~300 μm [24,40]) nucleated in the shot chamber, and small globular-rosette α-Al$_2$ grains (~10 μm [40]) nucleated in the die cavity. Conversely, it is generally accepted that agitation of the liquid during solidification facilitates dendrite fragmentation, which leads to grain refinement and morphological change [41–45]. Wu et al. [22] suggest that intensive shearing of the liquid during die-filling expedites the fragmentation of primary α-Al$_1$ crystals, leading to a high density of solid fragments in the liquid. If this is indeed the case, then surely grain size distributions in HPDC microstructures should be trimodal, rather than bimodal— i.e. they should comprise a mixture of primary α-Al$_1$ grains, primary α-Al$_2$ grains, and the fragmented den-

drite arms of primary α-Al$_1$ grains. This postulate forms the basis of the following discussion.

Univariate GMMs were fitted to the grain size distributions in Fig. 5(c,d) to identify subpopulations within each data set. Estimated AIC and BIC are shown in the supplementary material (see Fig. S8) and support the case of $k = 3$, indicating that both grain size distributions are trimodal. Although the flow field intensity appears to have a negligible influence on μ_1, an increase in ε is shown to produce a significant decrease in μ_3 (from 33.2 to 17.1 μm) and a modest decrease in μ_2 (from 12.5 to 8.8 μm). Additionally, the number fraction of grains in Component-2 increases from 0.45 (TRS) to 0.70 (LRS). This may be interpreted as the fragmentation of large primary α-Al$_1$ grains (μ_3) into more, smaller crystals (μ_2)—in this framework μ_1 represents primary α-Al$_2$ grains solidified in the die cavity. The observed refinement of μ_1 and μ_2 may be explained by considering the liquid temperature at the end of die-filling (Fig. 7): higher cooling rates are attained in the LRS casting than in the TRS casting, which may inhibit the growth of both primary α-Al$_2$ grains and fragmented α-Al$_1$ crystals.

We may divide dendrite fragmentation mechanisms into two broad classes, depending on the proposed driving force for breakage: those which rely on direct mechanical action of the hydrodynamic field to induce bending and subsequent fragmentation [41,42]; and those which depend on the induced movement of solute-rich liquid to destabilise the solid relative to the liquid [44,45]. Although there is compelling ex-

perimental evidence that primary α-Al$_1$ crystals bend plastically during HPDC [24], this is not necessarily evidence for a mechanical mode of breakage—how can we ascertain that crystal bending occurs prior to breakage, as opposed to during the intensification stage when a pressure of 30~100 MPa [12] is applied to the solidifying alloy? Previous studies based on synchrotron X-ray imaging [46] have demonstrated that the induced flow of inter-dendritic liquid may destabilise the local temperature-concentration-curvature equilibrium, leading to local remelting of the dendrite root. Adopting this framework, turbulent oscillations of the surrounding liquid may cause the local thermal and constitutional conditions to fluctuate intermittently, which may expedite the remelting process—the time scale of turbulence is likely to be smaller than that required for both thermal and constitutional equilibration. Clearly, much work needs to be done if we wish to understand this interesting phenomenon.

5. Conclusions

1 A novel technique, based on X-ray tomography and unsupervised machine learning, is presented that partitions inclusions into clusters based on their size, shape, and attenuating behaviour. From this, one can deduce the species of inclusions contained in a material and perform quantitative analyses on the individual phases.

2 In a turbulent flow, large non-metallic inclusions are broken down into more, smaller particles with a compact morphology. Increasing the dissipation rate of turbulent kinetic energy is shown to promote breakage, leading to an increase in tensile strength (mean: +16%) and tensile ductility (mean: +68%). It is proposed that breakage occurs in a manner analogous to the rupture of colloidal aggregates and highly viscous droplets suspended in a turbulent flow.

3 An increase in the dissipation rate of turbulent kinetic energy is also accompanied by a refinement of large primary α-Al$_1$ crystals nucleated in the shot chamber. Grain refinement is ascribed to the fragmentation of incipient grains induced by turbulent oscillations of the surrounding liquid.

Declaration of Competing Interest

The authors declare that they have no known competing financial interests or personal relationships that could have appeared to influence the work reported in this paper.

Acknowledgments

Data availability

The raw/processed data required to reproduce these findings cannot be shared at this time due to legal or ethical reasons.

Supplementary materials

Supplementary material associated with this article can be found, in the online version, at doi:10.1016/j.mtla.2021.101114.

References

[1] S. Wang, Y. Wang, Q. Ramasse, Z. Fan, The nature of native MgO in Mg and its alloys, Metall. Mater. Trans. A 51 (2020) 2957–2974.

[2] B. Lebon, H. Li, J. Patel, H. Assadi, Z. Fan, Numerical modelling of melt-conditioned direct-chill casting, Appl. Math. Model. 77 (2020) 1310–1330.

[3] E. Lordan, J. Lazaro-Nebreda, Y. Zhang, Z. Fan, Effective degassing for reduced variability in high-pressure die casting performance, JOM 71 (2019) 824–830.

[4] E. Koya, M. Nakagawa, S. Kitagawa, J. Ishimoto, Y. Nakano, N. Ochiai, Research of atomization phenomena in HPDC-step 1 feature of gas porosity dispersion and photography of atomized flow, SAE Tech. Pap. (2018) 1–8 1392.

[5] C. Tian, J. Law, J. van der Touw, M. Murray, J.Y. Yao, D. Graham, D. St. John, Effect of melt cleanliness on the formation of porosity defects in automotive aluminium high pressure die castings, J. Mater. Process. Technol. 122 (2002) 82–93.

[6] E. Lordan, J. Lazaro-Nebreda, Y. Zhang, K. Dou, P. Blake, Z. Fan, On the relationship between internal porosity and the tensile ductility of aluminium alloy die-castings, Mater. Sci. Eng. A 778 (2020) 139107.

[7] S. Ji, W. Yang, B. Jiang, J.B. Patel, Z. Fan, Weibull statistical analysis of the effect of melt conditioning on the mechanical properties of AM60 alloy, Mater. Sci. Eng. A 566 (2013) 119–125.

[8] Y. Zhang, J.B. Patel, J. Lazaro-Nebreda, Z. Fan, Improved defect control and mechanical property variation in high-pressure die casting of A380 alloy by high shear melt conditioning, JOM 70 (2018) 2726–2730.

[9] D. Eskin, I. Tzanakis, F. Wang, G.S.B. Lebon, T. Subroto, K. Pericleous, J. Mi, Fundamental studies of ultrasonic melt processing, Ultrason. Sonochem. 52 (2019) 455–467.

[10] N.G. Özcan-Taşkın, G. Padron, D. Kubicki, Comparative performance of in-line rotor-stators for deagglomeration processes, Chem. Eng. Sci. 156 (2016) 186–196.

[11] C. Gourlay, H. Laukli, A. Dahle, Defect band characteristics in Mg-Al and Al-Si high-pressure die castings, Metall. Mater. Trans. A 38 (2007) 1833–1844.

[12] X. Niu, K. Tong, B. Hu, I. Pinwill, Cavity pressure sensor study of the gate freezing behaviour in aluminium high pressure die casting, Int. J. Cast Met. Res. 11 (1998) 105–112.

[13] V. Becker, E. Schlauch, M. Behr, H. Briesen, Restructuring of colloidal aggregates in shear flows and limitations of the free-draining approximation, J. Colloid Interface Sci. 339 (2009) 362–372.

[14] K. Higashitani, K. Iimura, H. Sanda, Simulation of deformation and breakup of large aggregates in flows of viscous fluids, Chem. Eng. Sci. 56 (2001) 2927–2938.

[15] N. Zumaeta, E.P. Byrne, J.J. Fitzpatrick, Breakage of protein precipitates flowing through orifices, Chem. Eng. Res. Des. 86 (2008) 107–117.

[16] R. Sanjuan-Galindo, E. Soto, R. Zenit, G. Ascanio, Viscous filament fragmentation in a turbulent flow inside a stirred tank, Chem. Eng. Commun. 202 (2015) 1251–1260.

[17] M.U. Bäbler, M. Morbidelli, J. Bałdyga, Modelling the breakup of solid aggregates in turbulent flows, J. Fluid Mech. 612 (2008) 261–289.

[18] J. De Bona, A. Lanotte, M. Vanni, Internal stresses and breakup of rigid isostatic aggregates in homogeneous and isotropic turbulence, J. Fluid Mech. 755 (2014) 365–396.

[19] S. Blaser, Break-up of flocs in contraction and swirling flows, Colloids Surf. Physicochem. Eng. Asp. 166 (2000) 215–223.

[20] N. Zumaeta, G.M. Cartland-Glover, S.P. Heffernan, E.P. Byrne, J.J. Fitzpatrick, Breakage model development and application with CFD for predicting breakage of whey protein precipitate particles, Chem. Eng. Sci. 60 (2005) 3443–3452.

[21] D. Gunasegaram, M. Givord, R. O'Donnell, B. Finnin, Improvements engineered in UTS and elongation of aluminium alloy high pressure die castings through the alteration of runner geometry and plunger velocity, Mater. Sci. Eng. A 559 (2013) 276–286.

[22] M. Wu, X. Li, Z. Guo, S. Xiong, Effects of process parameters on morphology and distribution of externally solidified crystals in microstructure of magnesium alloy die castings, China Foundry 15 (2018) 139–144.

[23] ASTM E8-03, Standard Test Methods for Tension Testing of Metallic Materials, ASTM International, West Conshohocken, PA, 2003.

[24] S. Otarawanna, C. Gourlay, H. Laukli, A. Dahle, Agglomeration and bending of equiaxed crystals during solidification of hypoeutectic Al And Mg alloys, Acta Mater. 58 (2010) 261–271.

[25] K. Dou, E. Lordan, Y. Zhang, A. Jacot, Z. Fan, Numerical simulation of fluid flow, solidification and defects in high pressure die casting (HPDC) process, IOP Conf. Ser. Mater. Sci. Eng. 529 (2019) 012058.

[26] S. Elghobashi, T. Abou-Arab, A two-equation turbulence model for two-phase flows, Phys. Fluids 26 (1983) 931–938.

[27] A. Vakhrushev, A. Ludwig, M. Wu, Y. Tnag, G. Nitzl, G. Hackl, Modeling of Turbulent Melt Flow and Solidification Processes in Steel Continuous Caster with the Open Source Software Package, Open FOAM, 2010.

[28] O. Koser, J. Ruckert, P. Ubl, Modelling and Optimization of Part Ejection in Magnesium High Pressure Die Casting, ESI Group, 2015.

[29] H. Gjestland, S. Sannes, J. Svalestuen, H. Westengen, Optimizing the magnesium die casting process to achieve reliability in automotive applications, SAE Trans. 114 (2005) 67–73.

[30] R. Bergmann, A. Bill, On the origin of logarithmic-normal distributions: an analytical derivation, and its application to nucleation and growth processes, J. Cryst. Growth. 310 (2008) 3135–3138.

[31] M. Saeedipour, S. Schneiderbauer, S. Pirker, S. Bozorgi, A numerical and experimental study of flow behavior in high pressure die casting, Magnesium Technology (2014) 185–190.

[32] S. Coles, An Introduction to Statistical Modelling of Extreme Values, Springer-Verlag, 2001.

[33] Y. Liao, D. Lucas, A literature review of theoretical models for drop and bubble breakup in turbulent dispersions, Chem. Eng. Sci. 64 (2009) 3389–3406.

[34] P. Mallick, Materials, Design and Manufacturing for Lightweight Vehicles, Woodhead Publishing, 2010.

[35] J. McGonagle, G. Pilling, A. Dobre, V. Tembo, A. Kurmukov, E.R. Chumbley. Gaussian mixture model. *Brilliant.org*. Retrieved 22:20, May 14, 2021, from https://brilliant.org/wiki/gaussian-mixture-model/.

[36] Y. Zhang, S. Wang, E. Lordan, Y. Wang, Z. Fan, Improve mechanical properties of high pressure die cast Al9Si3Cu alloy via dislocation enhanced precipitation, J. Alloys Compd. 785 (2019) 1015–1022.

[37] S. Ji, W. Yang, F. Gao, D. Watson, Z. Fan, Effect of iron on the microstructure and mechanical property of Al-Mg-Si-Mn and Al-Mg-Si diecast alloys, Mater. Sci. Eng. A 564 (2013) 130–139.

[38] T. Mang, W. Dresel, Lubricants and Lubrication, John Wiley & Sons, 2007.

[39] ATC Europe, Lubricant Additives: Use and Benefits (2016). *Atc-europe.org.* Retrieved 22:26 May 14, 2021, from https://www.atc-europe.org/public/Document%20118%20-%20Lubricant%20Additives%20Use%20and%20Benefits.pdf.

[40] S. Otarawanna, C. Gourlay, H. Laukli, A. Dahle, Microstructure formation in $AlSi_4MgMn$ and $AlMg_5Si_2Mn$ high-pressure die castings, Metall. Mater. Trans. A 40 (2009) 1645–1659.

[41] R. Doherty, H. Lee, E. Feest, Microstructure of stir-cast metals, Mater. Sci. Eng. 65 (1984) 181–189.

[42] A. Vogel, Turbulent flow and solidification: stir-cast microstructure, Met. Sci. 12 (1978) 576–578.

[43] R. Mathiesen, L. Arnberg, P. Bleuet, A. Somogyi, Crystal fragmentation and columnar-to-equiaxed transitions in Al-Cu studied by synchrotron X-ray video microscopy, Metall. Mater. Trans. A 37 (2006) 2515–2524.

[44] D. Ruvalcaba, R. Mathiesen, D. Eskin, L. Arnberg, L. Katgerman, *In situ* observations of dendritic fragmentation due to local solute-enrichment during directional solidification of an aluminum alloy, Acta Mater. 55 (2007) 4287–4292.

[45] D. Shu, B. Sun, J. Mi, P. Grant, A high-speed imaging and modeling study of dendrite fragmentation caused by ultrasonic cavitation, Metall. Mater. Trans. A (2020).

[46] E. Liotti, A. Lui, R. Vincent, S. Kumar, Z. Guo, T. Connolley, I.P. Dolbnya, M. Hart, L. Arnberg, R. Mathiesen, P. Grant, A synchrotron X-ray radiography study of dendrite fragmentation induced by a pulsed electromagnetic field in An Al-15Cu alloy, Acta Mater. 70 (2014) 228–239.